JOURNAL OF MATERIALS SCIENCE **25** (1990) 4285–4297

Relation between tensile properties and microstructure in type 316 stainless steel SA weld metal

G. PIATTI, M. VEDANI
Materials Performance and Reliability Division, Advanced Materials Institute,
Ispra Establishment, Joint Research Centre, Commission of the European Communities,
21 020 Ispra, Italy

Tensile properties of a thick, multipass, submerged-arc (SA) weld-deposited type 316 are investigated by tests at room temperature and at 400° C and by microstructural and compositional analyses. The as-deposited metal, which shows a lower yield strength, a comparable ultimate tensile strength and a lower total elongation compared to the (solution-annealed) parent metal, is characterized by systematic variations in tensile properties across its thickness, with the highest strength and the lowest ductility in the weld centre. These variations are related to material variability (mainly changes in dislocation density) within the weld metal due to local dissimilarities in thermal and mechanical histories during welding.

1. Introduction

The design, prediction of performance, and safety analysis of austenitic stainless steel welded components, such as those needed in advanced nuclear systems (for instance, the primary containment in liquid metal fast breeder reactors (LMFBR) or first-wall structures in tokamak fusion devices), require a complete knowledge of their physical and mechanical properties. Unfortunately, whilst much information on the mechanical characteristics of austenitic stainless steel welds has been obtained from (transverse to weld) composite specimens, only little or even no data are available on the mechanical behaviour of the individual zones of the welded joint (parent metal, heat-affected zone (HAZ) and weld-deposited metal) as shown in literature reviews [1, 2]. In particular, it would be useful to have at one's disposal more information on the mechanical properties of the weld-deposited metal as influenced by its material variability. This is characterized by microstructural variations:

(a) between the parent metal (usually fully austenitic) and the weld metal (containing various amounts of δ-ferrite retained at room temperature) [1–4]. The presence of δ-ferrite in the austenite matrix is necessary to prevent cracking during welding according to a well-established practice;

(b) within the weld-deposited metal from one point to another in the dislocation density, in the columnar grain size, in the substructure size, in the content, distribution and morphology of δ-ferrite or other phases eventually present as carbides, or σ-phases, and in the chemistry (adjustment by filler metal) [3–9]. In particular, in the case of a heavy section (thickness 25 mm) of austenitic weld deposit, when the number of welding passes is considerable, the variations in the dislocation density from the surface to the centre of the weld are enhanced [10, 11].

The above microstructural and compositional variability was confirmed previously [12] on a weld deposit from a weld prepared by joining 50 mm thick type 316 stainless steel (vessel) plates with a multipass submerged-arc weld. With a view to assess the effect of the above variability (within the weld) on the time-independent (tensile) behaviour of the weld-deposited metal itself, a further study was performed on the same type 316 stainless steel SA weld generating tensile data at room and high temperatures from all-weld specimens taken from various locations across the weld metal, and evaluating the factors which influence the deformation and fracture behaviour by microstructural and compositional analyses. The results are presented and discussed here.

2. Material

The base material for the present study was a type 316 stainless steel supplied by Uddeholm (Sweden) as a 50 mm thick solution-annealed plate (heat LK 4290). The chemical analysis is given in Table I. The steel is characterized by a high nitrogen level, a relatively low carbon level and strict limitations in impurities which are supposed to increase mechanical properties and improve weldability, in accordance with the specifications proposed by Wood [13] for type 316 stainless steel to be used in LMFBR systems. The microstructure proved to be fully austenitic with an approximately equiaxed grain size of 90 μm and a Vickers hardness (10 kg load) of 215 kg mm^{-2}. There were non-metallic inclusions (alumina and globular oxides) and no carbide precipitates were observed. This heat has been previously extensively tested on its tensile behaviour over a large strain-rate range (1×10^{-5} to 1×10^{-2} sec^{-1}) and for a variety of temperature conditions (20 to 800° C) [14–16].

The weld was made by Zanon (Italy) with an auto-

0022–2461/90 $03.00 + .12

TABLE I Chemical composition (wt %) of materials tested [12]

Material	Cr	Ni	Mo	C	N	Si	Mn	P	S	Ti	Nb	Cu	Fe
AISI 316													
As-received	16.9	12.3	2.48	0.052	0.082	0.34	1.67	0.020	0.009	0.006	0.008	0.007	rest
Solution annealed													
(50 mm thick) plate													
Weld material													
Root deposit	17.80	11.75	2.49	0.03	0.07	0.48	1.52	0.031	0.027	0.003	0.012	0.005	rest
Front-pass deposit	17.33	11.24	2.54	0.03	0.07	0.67	0.99	0.037	0.029	0.003	0.009	0.092	rest
Back-pass deposit	17.24	11.08	2.63	0.03	0.07	0.65	0.97	0.035	0.028	0.003	0.009	0.125	rest

matic SA machine by joining along the longest side some sections (1260 mm × 300 mm × 50 mm) cut from the plate. A joint configuration, symmetrical double U-groove, was adopted and a multipass procedure (28 passes) was chosen because of the large thickness (50 mm) of the plate. Two type 316 L commercial filler metals were used with compositions adjusted to match the base metal in order to obtain in the weld-deposit compositions characterized by a volume per cent of δ-ferrite between 3 and 8, as required by established practice to prevent hot cracking [17]. The welding conditions are given in Table II. More details concerning the welding procedure are reported in the investigation mentioned previously [12].

A satisfactory weld soundness was found by conventional non-destructive testing (fluorescent penetrant liquid method and radiographic examination). However, because of the poor inspectability of austenitic stainless steels, it is difficult to detect such defects as microporosities, which could, however, be present. Finally, no post-weld heat treatment was performed.

Exhaustive details of the macro- and microstructures of the weld-deposited metal are available [12], but the features more relevant to the present study can be summarized and illustrated briefly by:

(a) a view of the weld cross-section (Fig. 1) which may be characterized by an approximate hour-glass shape of the weld deposit, not symmetrical over the mid-plane of the plate, through a build-up of the successively overlaid weld beads reflecting the multipass procedure, and by a macrostructure which consisted of long columnar grains;

(b) a solidification substructure of the weld which was mainly cellular or cellular–dendritic and no presence of equiaxed grains;

(c) a duplex (γ-austenite matrix plus δ-ferrite second phase) microstructure (Fig. 2a) which was characterized by vermicular ferrite located at the cell axes as a result of ferritic–austenitic solidification followed by a solid-state δ–γ transformation. However, some areas of the weld deposit in the root region solidified with a final morphology (Fig. 2b) which was characterized by a distribution of δ-ferrite at the cell-boundaries after austenitic–ferritic solidification.

TABLE II Welding parameters [12]

Process	Submerged-arc welding*
Joint design	Double U-groove
Number of passes	28
Interpass temperature	55° C (max)
Post heat	None
Electrode wire	2.4 and 3.25 mm diameter
Flux	Neutral
Current	280 to 340 A
Voltage	30 V
Travel speed	45 to 58 cm min^{-1}
Heat input rate	1.05 to 1.12 MJ m^{-1}

*First pass made by shielded metal-arc welding.

3. Experimental procedure

Cylindrical tensile specimens were machined from several sections of the welded joint described above, parallel to the weld direction (all-weld specimens) at various distances from the weld centre according to the sampling location of Fig. 3. Standard specimens (diameter 10 mm and gauge length 50 mm) indexed B and C, and small specimens (diameter 4 mm and gauge length 20 mm) indexed D and E were prepared. The latter specimens were used because of the restricted width of the root deposit region. The choice of the position of specimen D at 5 mm from the weld axis (front-pass side) was justified by a local relatively brittle area of structural significance, characterized by

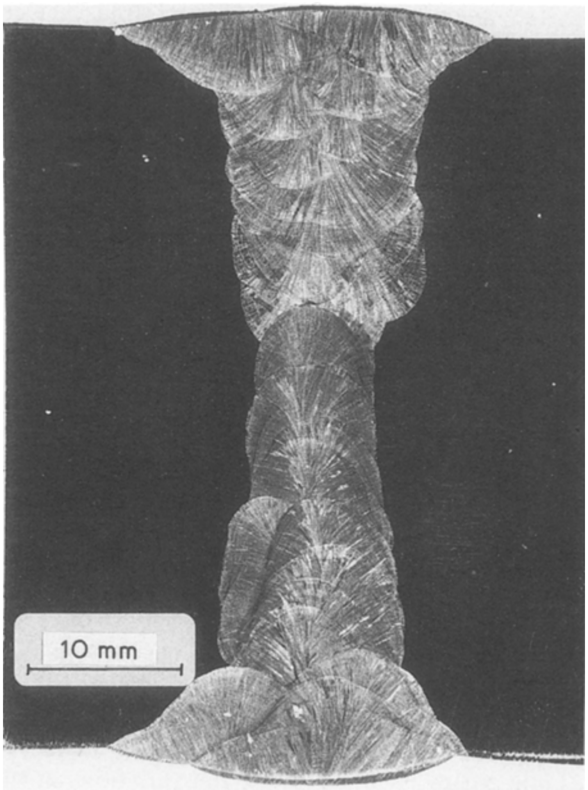

Figure 1 Macroetched view of cross-section from type 316 stainless steel SA weld joint [12].

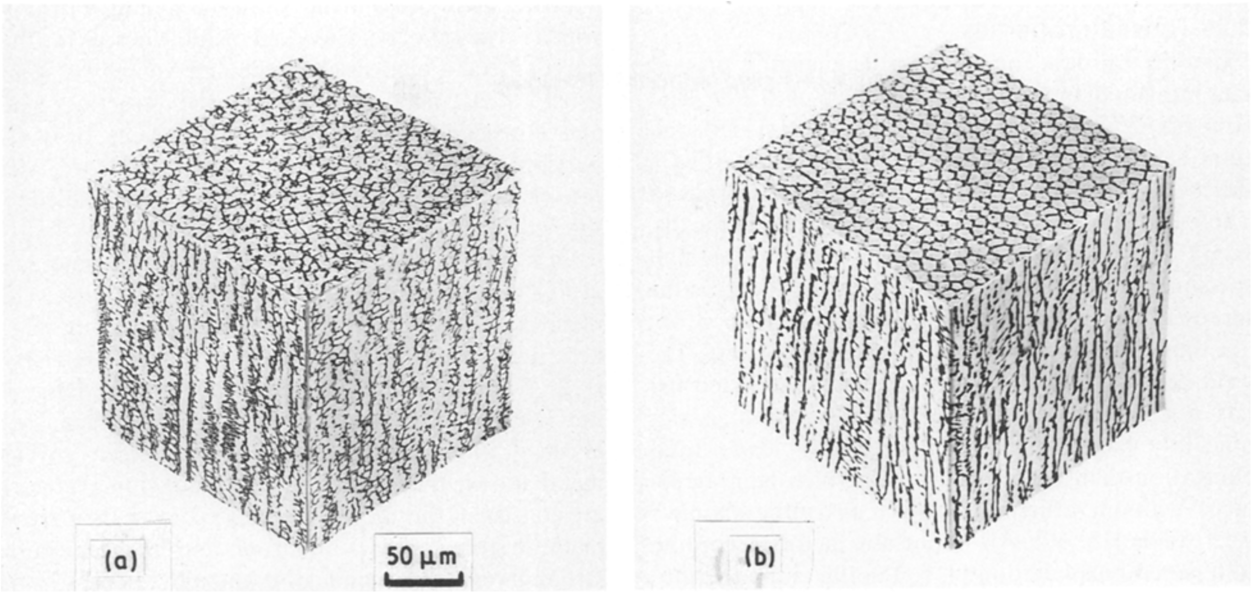

Figure 2 Three-dimensional composite micrographs of the ferrite morphology in type 316 stainless steel SA weld-deposit: (a) vermicular δ-ferrite (dark etching) located at the cell axes (ferritic–austenitic solidification mode); (b) vermicular δ-ferrite (dark etching) distributed at the cell-boundaries (austenitic–ferritic solidification mode). The δ-ferrite alignment is in the cellular or cellular–dendritic growth direction which is also the heat flow direction.

very high HV10 hardness values ranging from 284 to 296 kg mm^{-2}, whereas in the other areas of the weld metal the hardness (HV10) ranged from 230 to 270 kg mm^{-2} (Fig. 13 of [12]). Additional standard tensile specimens, indexed A, were machined from an unaffected region away from the weld (parent metal specimens).

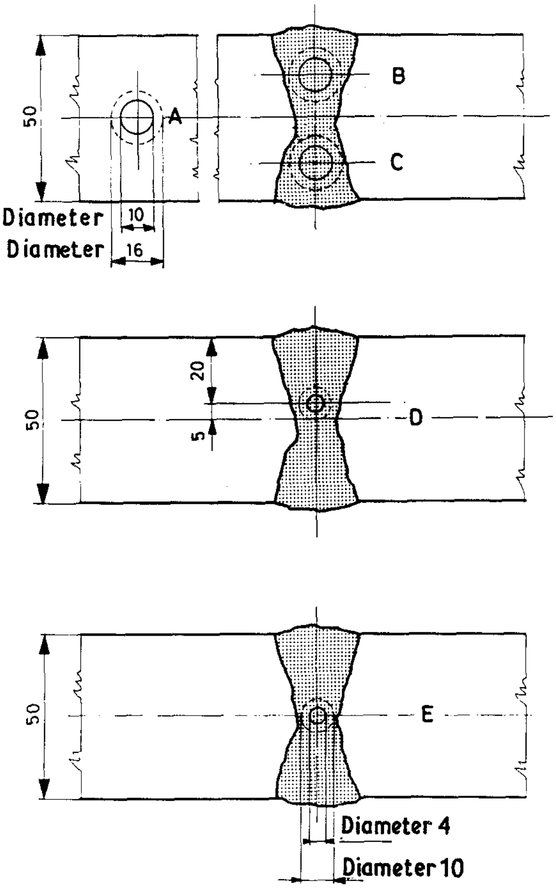

Figure 3 Location of standard (A, B, C) and small (D, E) tensile specimens. Hour-glass-shaped region represents type 316 stainless steel SA weld-deposited metal. Dimensions in mm.

Tensile tests were performed by a Schenk-Trebel RM 100 electro-mechanical machine at room temperature and at 400° C, and over a strain-rate range of 1×10^{-4} to 1×10^{-2} sec^{-1} for the standard specimens, and at a single strain-rate of 1×10^{-3} sec^{-1} for the small specimens. All the specimens were pulled to fracture at a constant extension rate. Specimen deformation was monitored during the test using an inductive extension sensor for accurate strain measurements. The tests at 400° C were run in air in a tubular electrical-resistance type furnace with a temperature along the gauge length of the specimen maintained within $\pm 2°$ C. The choice of 400° C ($\simeq 0.40\ T_f$, where T_f is the absolute melting temperature) for the hot tests was made because data related solely to time-independent behaviour of the material were required. In fact, at temperatures above 400° C the time-dependent behaviour becomes significant in type 316 stainless steel and superposition with time-dependent behaviour could occur.

Transverse and longitudinal sections, cut from halves of selected broken specimens, were prepared by mechanical polishing and electrochemical etching (10% oxalic acid or 50% HNO_3 solution) for metallographic examination (Leitz MM 6 optical microscope). The fracture surface was investigated by scanning electron microscopy (Philips SEM 505) in order to assess the fracture mode. Chemical microanalyses were carried out using an EDAX detector fitted to the Philips SEM 505.

Finally, TEM analyses were also used in selected deformed specimens. Thin foils were taken from longitudinal sections and prepared by electropolishing to perforation in a 70 : 15 : 15 acetic acid : perchloric acid : ethanol (by volume) electrolyte with initially 37 V and in the final part of the preparation with 30 V. Lastly the ferrite (volume) content was evaluated in selected specimens using a permeability meter (Fisher ferrite scope).

4. Results and discussion

4.1. Tensile properties

Experimental data for the usual engineering properties measured in a tensile test, such as 0.2% yield strength (YS), ultimate tensile strength (UTS) and total elongation to fracture (e_f), are illustrated as a function of the test temperature and strain-rate in Table III for the standard specimens A (parent metal), B, C (front- and back-pass deposits) and for the small specimens D and E (root-pass deposit). Each value represents the average from at least two tests.

Compared with weld and parent metal data, the weld-deposited metal (front- and back-pass deposits) has a comparable ultimate tensile strength, a significantly higher yield strength and a lower total elongation than the parent metal, which is in agreement with literature reviews on austenitic stainless steel welds [18, 19]. An important factor, according to a general explanation [4, 5, 18, 19], is the thermomechanical effects during welding which induce considerable deformation and a worked final microstructure. Ward [4] has estimated the tensile characteristics of a multipass gas–tungsten arc-deposited type 316 stainless steel to be consistent with those of an equivalent steel in 7% to 8% cold-worked conditions. Further information on the strain-hardened state in the present weld deposit can be obtained from the 0.2% YS/UTS ratio values also listed in Table III. Front- and back-pass deposits are characterized by high YS/UTS values included in the ranges 0.78 to 0.81 and 0.72 to 0.79 at room temperature and at high temperature, respectively, whereas in the case of the base metal, the YS/UTS ratios are considerably lower (0.42 to 0.51 and 0.30 to 0.34 at room temperature and at high temperature, respectively). The above features indicate a low weld-metal strain-hardening capacity which is typical of cold-worked metal, whereas for the parent metal a high strain-hardening capacity is seen, as expected from a solution-annealed structure. The above observations are also justified when, for comparison with weld metal and parent metal, we take into account the data of Table III which are related to the root deposit region of the weld metal.

Other factors which contribute to the differences in yield strength and ductility between parent and weld metal could be found in a strengthening effect in weld-deposited metal of δ-ferrite and/or of the chemistry [1, 2]. δ-ferrite strengthening, as will be shown later, is not relevant in the present case, whereas chemistry effects (differences in composition between parent metal and weld-deposited metal as shown in Table I) are consistent but they are in the favour of the parent metal (higher contents of carbon and nitrogen, both strong interstitially solid-solution strengtheners [20]). This should be considered in the sense that it tends to balance the strengthening effect of thermal cycling and so reduces the differences in the corresponding tensile properties of the parent and the weld metal.

Comparising front-pass, back-pass and root deposits, it is evident from Table III that, for the investigated single strain rate of $\dot{\varepsilon} = 1 \times 10^{-3}\,\text{sec}^{-1}$, the root deposit YS and UTS exceed the front-pass and back-pass deposit YS and UTS, respectively, whereas the root deposit e_f is lower than the front-pass and back-pass deposit e_f. On the contrary, the YS, UTS and e_f data for the front-pass and back-pass deposits are nearly equal to both temperatures and at all strain rates investigated. The above significant differences between front- and back-pass deposit data, on the one hand, and root-pass data on the other, are generally

TABLE III Tensile properties of all-weld metal and parent metal specimens

Specimen location	Temperature (°C)	Strain rate (sec^{-1})	0.2% yield strength (MPa)	Ultimate tensile strength (MPa)	YS/UTS ratio	Total elongation (%)
Front-pass deposit	B 20	1×10^{-2}	477	590	0.81	36.8
	B 20	1×10^{-3}	470	585	0.80	45.5
	B 20	1×10^{-4}	465	592	0.79	40.6
Back-pass deposit	C 20	1×10^{-2}	475	598	0.79	37.1
	C 20	1×10^{-3}	470	591	0.80	42.1
	C 20	1×10^{-4}	468	603	0.78	46.1
Front-pass deposit	B 400	1×10^{-2}	351	445	0.79	26.7
	B 400	1×10^{-3}	352	455	0.77	27.4
	B 400	1×10^{-4}	358	483	0.74	28.3
Back-pass deposit	C 400	1×10^{-2}	349	453	0.77	26.4
	C 400	1×10^{-3}	352	472	0.75	28.3
	C 400	1×10^{-4}	359	497	0.72	28.8
Root deposit*	D 20	1×10^{-3}	575	656	0.88	27.8
	E 20	1×10^{-3}	615	670	0.92	37.5
	D 400	1×10^{-3}	459	507	0.91	16.0
	E 400	1×10^{-3}	440	487	0.90	31.0
Base metal	A 20	1×10^{-2}	300	588	0.51	53.6
	A 20	1×10^{-3}	277	587	0.47	61.8
	A 20	1×10^{-4}	252	598	0.42	75.7
	A 400	1×10^{-2}	163	482	0.34	44.3
	A 400	1×10^{-3}	155	495	0.31	47.7
	A 400	1×10^{-4}	152	512	0.30	48.6

*Data for small specimens.

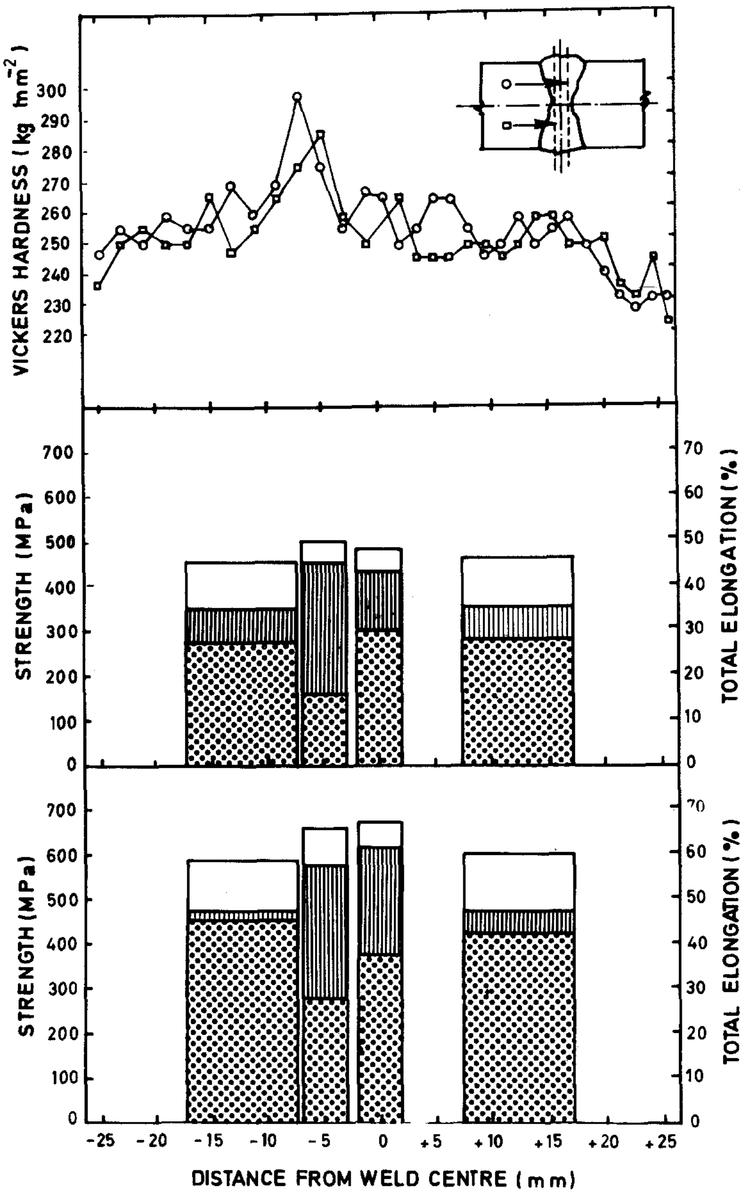

Figure 4 All-weld metal tensile characteristics (UTS, white; YS, striped, e_f dotted) at room temperature (bottom) and at 400° C (middle) and hardness (HV10) values (top) plotted along the type 316 stainless steel weld thickness.

observed in multipass austenitic stainless steel welds [3-5, 8, 10, 11] and have been explained in terms of thermal stresses occurring in welding which produce significant deformations in inner beads with increased dislocation density in the root region because of the fact that more thermal cycles are experienced by this region as compared to other regions. This explanation is fully valid also in the present case because other types of possible influence, such as those mentioned in Section 1 (variation in columnar grain size, etc.), are of minor importance in the present work, as will be discussed later. It should be noted that the large variations in YS and UTS from the surface to the centre of welds are in agreement with the hardness profile variations as seen in Fig. 4 where the tensile property values of Table III, corresponding to specimens B, C, D and E, fractured at room and high temperature and at $\dot{\varepsilon} = 1 \times 10^{-3}\,\text{sec}^{-1}$, are replotted as a function of weld thickness, together with the Vickers hardness (HV 10) values reported previously [12]. Generally, the room-temperature hardness data can be considered as a strength evaluation [21]. However, in the present case, the correlation between hardness and strength values is not as strict as expected according to the literature. In fact, the maximum in hardness ($297\,\text{kg}\,\text{mm}^{-2}$) at 5 to 7 mm from the weld centre does not coincide, as far as the position along the weld thickness is concerned, with the maximum (670 MPa) in strength, but rather with the minimum in ductility ($e_f = 16\%$), which confirms the relative brittleness of the area at 5 mm from the centre, previously revealed [12]. Moreover, it is to be noted that the above comparison between front- and back-pass deposits, on the one hand, and the root deposit on the other, is based on data obtained from specimens of different size. The literature indicates that there is an increase in flow stress with decreasing specimen diameter, generally accounted for by the increase in surface layer stress [22], whereas at the same time the decrease in ductility, which occurs because the component of the elongation-to-fracture contributed by necking (the other component has ability to elongate uniformly), is relatively higher for larger size specimens [23]. This means that the differences between small specimens (D, E) and standard specimens (B, C) are in reality less than appears from the data themselves for both strength and ductility, even if it is very difficult to give a quantitative evaluation of those differences.

4.2. Strain-rate influence

Table III shows for the weld-deposited metal (front- and back-pass deposit specimens) that the strength (UTS and YS) and ductility are insensitive to strain-rate changes over the rate range investigated at both test temperatures because the variations observed are in the range of normal data scatter. The present results, even if related to a narrow range of 1×10^{-4} to $1 \times 10^{-2}\ \mathrm{sec}^{-1}$, confirm previous data of Streichen and Ward [5] indicating a strain-rate insensitivity of the tensile properties of type 308 stainless steel weld metal at test temperatures below 538° C and over a strain-rate range of 1×10^{-5} to $1 \times 10^{-1}\ \mathrm{sec}^{-1}$. The above results suggest that the austenitic weld metal must be treated in a structural calculation for service conditions at room temperature as rate-independent material. On the contrary, the data of strength (YS) and ductility in Table III related to the parent metal show a rate dependence at room temperature which is in agreement with Ispra's previous results on various solution-annealed type 316 stainless steel [14–16, 24], showing a dynamic hardening as in the present case over large variations in strain rate (from 1×10^{-5} to $1 \times 10^{-2}\ \mathrm{sec}^{-1}$).

4.3. Macrostructure

The more streaking feature is the presence of an elliptical cross-section in the fractured all-weld metal specimens indicating an allotropic deformation behaviour at both test temperatures which is similar to that reported in the literature for other austenitic welds [1, 3, 9, 10]. In practice, the initial circular specimen cross-section was gradually distorted into an elliptical one during plastic deformation. Moreover, metallographic analyses of the microstructure in various cross-sections yielded evidence of a columnar grain growth direction parallel to the minor axis of the ellipse, and solute bands parallel to the major axis. The above observations confirm that anisotropic behaviour could be a result of local substructure orientations and preferred crystallographic orientations, as previously suggested [1, 3, 9, 10]. Both orientations develop during solidification as a result of a competitive growth process [25] which, in the present weld, was controlled by a "tear-drop" shaped weld-pool geometry, as previously shown [12]. According to the literature [25–27], this type of weld-pool morphology, which is characterized by straight columnar grains as shown in Fig. 5, should favour the above preferred orientations which, in turn, result in a marked anisotropy during deformation and affect the weld mechanical properties after welding. Another observed feature directly related to the influence of the anisotropic deformation is the occurrence of non-uniform diametral reductions in some deformed specimens in several austenitic welds, as previously observed by other authors [1, 3]. It should be noted that no features depending on anisotropic behaviour were observed in the parent metal, as expected.

The above "tear-drop" shaped weld pool is also not favourable as far as macro-segregation phenomena are concerned because it could enhance the levels of solute and impurities at the weld centre (Fig. 5) when the two solidification fronts from opposite sides impinge, according to Savage *et al.'s* model of the solidification process in welding [25]. These centre-line solute and impurity accumulations could be the cause of the formation of the area of relative brittleness or weakness mentioned previously which affected the toughness of the weld deposit (Fig. 4).

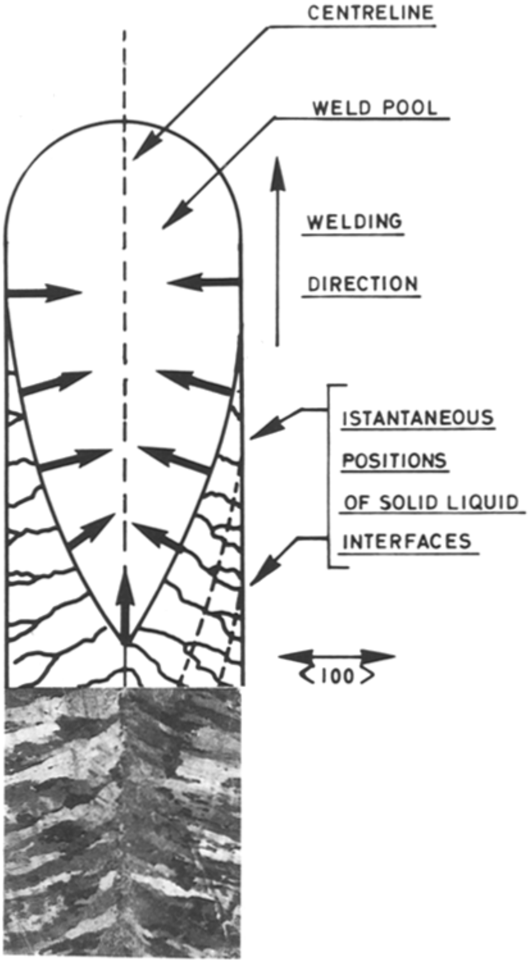

Figure 5 View of the (etched upper side) weld surface of the type 316 stainless steel weldment, showing columnar development typical of a tear-drop shaped weld-pool with cells growing perpendicular to fusion line in the plane of the sheet. ⟨1 0 0⟩ is the preferred orientation of the cellular substructure.

4.4. Microstructure

The structure observations on a microscopic scale are illustrated in Figs 6 and 7 (optical micrographs) and Fig. 8 (TEM) images. Fig. 6 shows various deformation microstructures seen in the fracture zones of specimens taken from different regions in the weld-deposited metal and fractured under different experimental conditions. The microstructures of Figs 6a and b originated from tensile deformation of microstructures similar to that of Fig. 3a, that is, those constituted by a cellular or cellular–dendritic morphology with δ-ferrite located at the cell axes as a result of a ferritic–austenitic solidification followed by a solid-state δ–γ transformation, according to Suutala *et al.'s* solidification model in austenitic stainless steel welds [28]. Most of the present weld (about 90%) solidified with this morphology [12]. The vermicular ferrite appears after large deformation in the necked zone near to fracture, elongated to a high degree in the

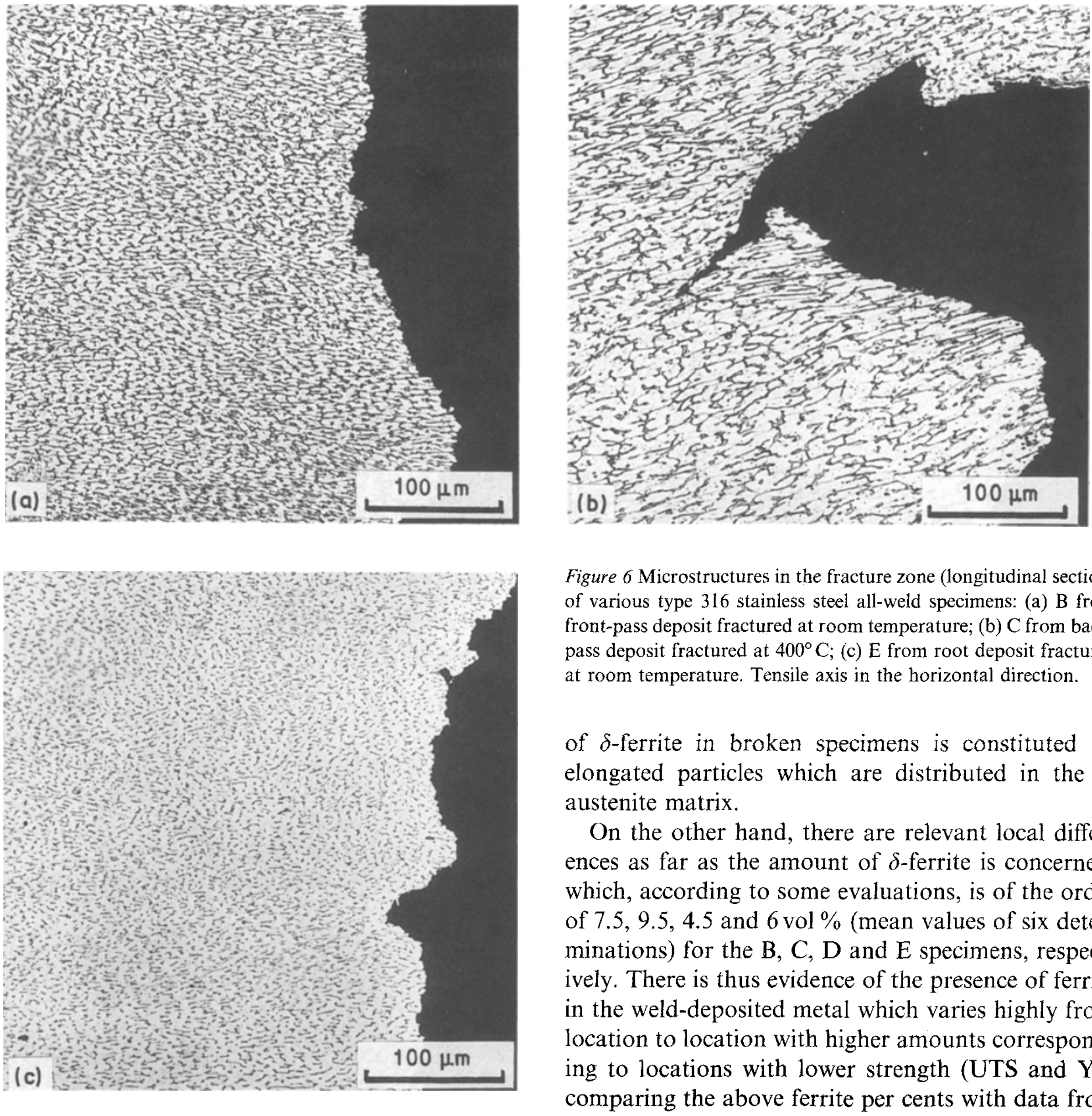

Figure 6 Microstructures in the fracture zone (longitudinal section) of various type 316 stainless steel all-weld specimens: (a) B from front-pass deposit fractured at room temperature; (b) C from back-pass deposit fractured at 400° C; (c) E from root deposit fractured at room temperature. Tensile axis in the horizontal direction.

tensile axis direction at both room (Fig. 6a) and high (Fig. 6b) temperature, indicating a large deformability of the δ-ferrite phase. Lastly, in the case of the ferrite morphology constituted by vermicular δ-ferrite located at the cell-boundaries (Fig. 3b), found mainly in the root-deposit region, there is also evidence of morphological variations after large specimen deformation (Fig. 6c), because the δ-ferrite appears in the form of elongated particles. However, this is not surprising, because the δ-ferrite at the boundaries of the cells (Fig. 3b) is not continuous [29] and this fact makes the morphological transformations from Fig. 3b to Fig. 6c during tensile deformation easier. On the contrary, in the particular case of specimen D, broken at 400° C after a limited deformation ($e_f = 12\%$) and little necking ($\sim 43\%$), the δ-ferrite morphology appears slightly modified (Fig. 7) and the cellular structure has undergone limited damage (Figs 7b and c). It is thus evident that the degree of elongation in the ferrite morphology is correlated with the degree of plastic deformation, and that the variations in the two δ-ferrite morphologies in the weld-deposited metal disappear at large plastic deformation, in the sense that in both cases the final morphology of δ-ferrite in broken specimens is constituted by elongated particles which are distributed in the γ-austenite matrix.

On the other hand, there are relevant local differences as far as the amount of δ-ferrite is concerned, which, according to some evaluations, is of the order of 7.5, 9.5, 4.5 and 6 vol % (mean values of six determinations) for the B, C, D and E specimens, respectively. There is thus evidence of the presence of ferrite in the weld-deposited metal which varies highly from location to location with higher amounts corresponding to locations with lower strength (UTS and YS) comparing the above ferrite per cents with data from Fig. 4. In the literature there are few cases of austenitic welds with a decrease in strength (UTS and YS) with increasing ferrite content [6, 30] whereas, in the majority of cases, the effect of the content of δ-ferrite is that it increases the YS and UTS, as in the case of more conventional wrought (unwelded) austenitic structures. The strenghening effect of the δ-ferrite is probably due to dispersion hardening mechanisms [4, 31, 32]. Probably, in the present weld, the morphology of the δ-ferrite, which is of the dendritic type, is not suitable for a dispersion hardening mechanism to occur, as is the globular δ-ferrite present in some austenitic welds [4].

The metallographic analysis also gives some information on the columnar grain size whose local variations across the weld metal thickness can be an important component of material variability, as mentioned above. Figs 7b and c show that in the root deposit it is of the order of 100 μm. This is in agreement with the grain size of the parent metal which is of the order of 90 μm [12] and it can be explained by the fact that the mode of weld-pool solidification controls the size and the pattern of solidified grains [25, 26]. More precisely, the moving pool of molten metal (Fig. 5) solidifies within the joint by epitaxial growth from crystals favourably oriented at the initial solid/liquid interface and from bead to bead through a competitive process (Fig. 1); consequently, the initial dimensions of the parent grain size do not vary significantly.

The thin-foil examination performed in the present work is related to different locations in the weld-deposited metal (as-welded material and selected all-weld specimens fractured at room temperature). Generally, weld-deposited metal (as-welded material) viewed through the TEM, appears (Fig. 8a) as a dislocation substructure with an important network of low-angle subgrain boundaries. These were formed in the course of the rapid weld-pool solidification because of an accommodation process of the mismatch between adjacent δ-ferrite dendrites, according to a TEM analysis in a 16–8–2 austenitic weld [8]. The size of these subgrains is comparable, as shown previously [9], to secondary-arm dendrite spacing which, in the present weld, has been roughly estimated to vary from about 10 μm in front-pass and back-pass deposits to about 3 μm in the root-pass deposit. The dislocation density is higher in the γ-austenite matrix than in the δ-ferrite second phase (Fig. 8a) and increases gradually from the surface to the centre of the weld deposit. The latter feature confirms the above-mentioned suggestion of an increased dislocation density in the root region because of more thermal cycles experienced in this region. Fig. 8a also shows that in some areas there is evidence of round inclusions (Fig. 8a) whose composition has not been identified. However, according to microcompositional EDX analysis of similar particles on fracture surfaces of several broken specimens, these inclusions could be assessed as deoxidation products (see later). After (room-temperature) deformation the austenitic areas are characterized by a dislocation cell structure (Fig. 8b) and also by slip bands. The dislocation density and deformation in ferrite are as important as in austenite. These observations are in agreement with previous TEM analyses on austenitic welds [6–9, 33, 34].

Finally, the effects due to variations in chemical composition might have an importance; however, in the present work (see Table I) there are no differences of practical significance among the chemical analyses of front-pass, root-pass and back-pass deposits, especially as far as nitrogen and carbon are concerned which are the only alloying elements characterized by a strong solution strengthening of austenitic stainless steels, as previously mentioned.

4.5. Fracture

Metallographic and SEM evidence shows that the fracture behaviour of the broken specimens can be considered ductile. A cup and cone appearance on a

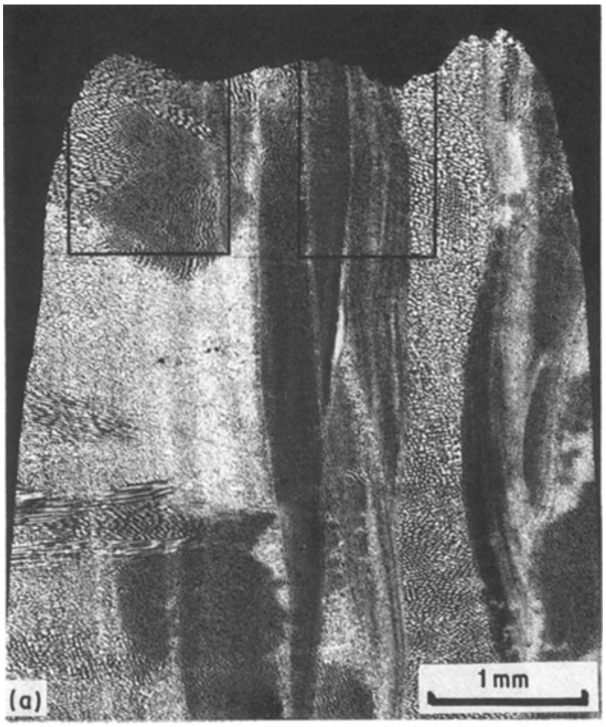

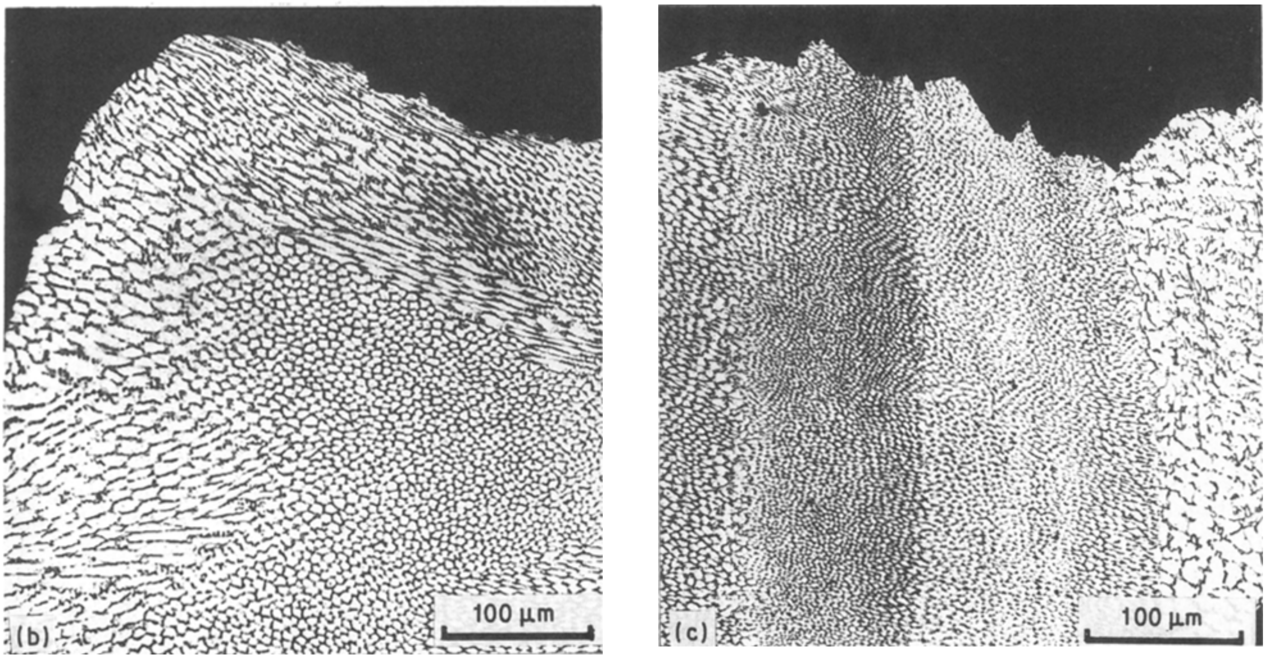

Figure 7 Microstructures of a longitudinal section of specimen E from type 316 stainless steel root-pass deposit fractured at 400° C: (a) gauge length and fracture zone; (b) and (c) areas of fracture zone (a) at higher magnification. Tensile axis in vertical position.

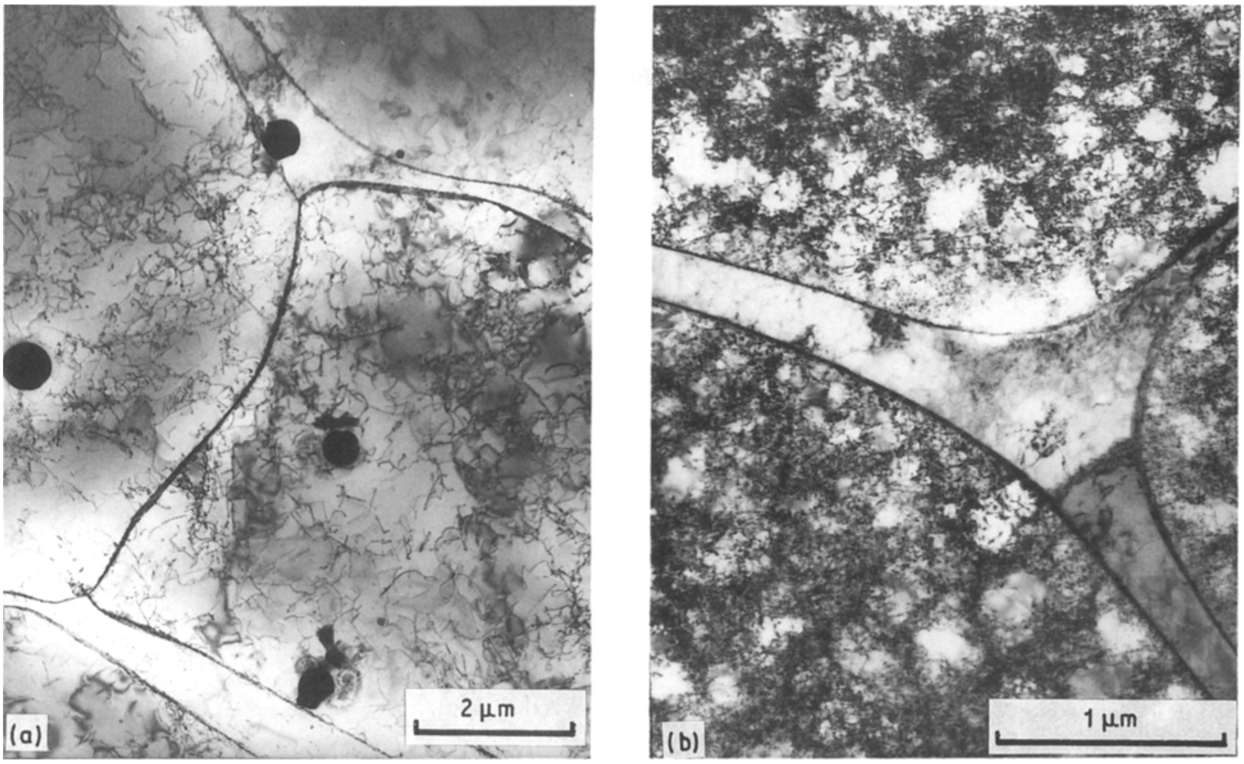

Figure 8 Transmission electron micrographs from SA type 316 stainless steel weld deposit: (a) root-pass deposit (as-welded); (b) specimen C deformed at room temperature.

macroscopic scale with a predominance of a cone or shear portion (due to the fact that there are no microfissures in the fracture zone, as shown in Fig. 6), is accompanied on a microscopic scale by dimples, as shown in the SEM images of Fig. 9. The dimples are associated with impurity particles which are generally round and have various different sizes (Fig. 9). Void nucleation occurred by impurity particle/matrix interface separation controlled by the plastic flow of the austenite matrix. Void growth was also governed by plastic deformation, as suggested by fine wavy markings in the cavity and near to the cavity, which can be explained as a result of slip on many favourably oriented planes according to Beachem and Heyn [35]. Coalescence by internal necking of cavities (Fig. 9) is the third stage which characterizes the fracture behaviour in the present austenitic weld metal, which is in agreement with microstructural aspects of the ductile fractures of the metal recently reviewed [36, 37].

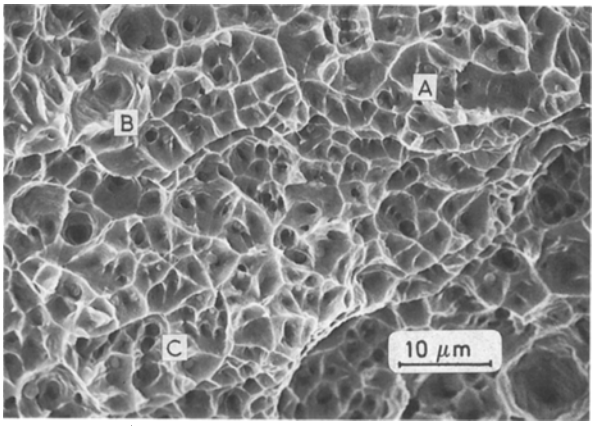

Figure 9 Fracture surface (SEM image) of type 316 stainless steel front-pass deposit B specimen fractured at room temperature: areas marked A, B and C show void nucleation at a particle/matrix interface, void growth by plastic flow (fine wavy slip lines) and void coalescence by internal necking, respectively.

The above fracture behaviour is typical of the all-weld specimens B and C from front- and back-pass deposits and also with a minor degree of the ductility of specimens E from the root deposit. On the contrary, for the specimens D, from a localized area in the root deposit at 5 mm from the centre, the fracture behaviour changes at the macroscopic level, whereas at the microscopic level it remains always ductile. In fact, there is an enlargement of the cup or flat portion of the fracture surface and a strong diminution of the cone or shear portion, as shown in the micrograph of Fig. 7 of a longitudinal section of a specimen broken at 400° C and characterized by a low total elongation value (12%). The fracture surface of the same specimen is shown in the SEM images of Fig. 10. Dimples are always present but some areas of the surface are characterized by deep, parallel and adjoining striations (Fig. 10a) originated by a process of coalescence of aligned microvoids nucleated at impurity particles (Fig. 10b). The results of the EDX analyses (for elements heavier than sodium) indicated that inclusions analysed contained silicon, sulphur, chromium, manganese, iron and nickel. The majority of inclusions are manganese-rich and originate from deoxidation products. This analyses is similar to that performed on other stainless steel weld metals [38–40]. In our opinion the above inclusions or impurities must be related to the macrosegretation phenomena occurring in the grain boundary by impingement (Fig. 5) which produce an area of relative weakness, as assessed by tensile and hardness tests (Fig. 4). This area leads to an anticipated

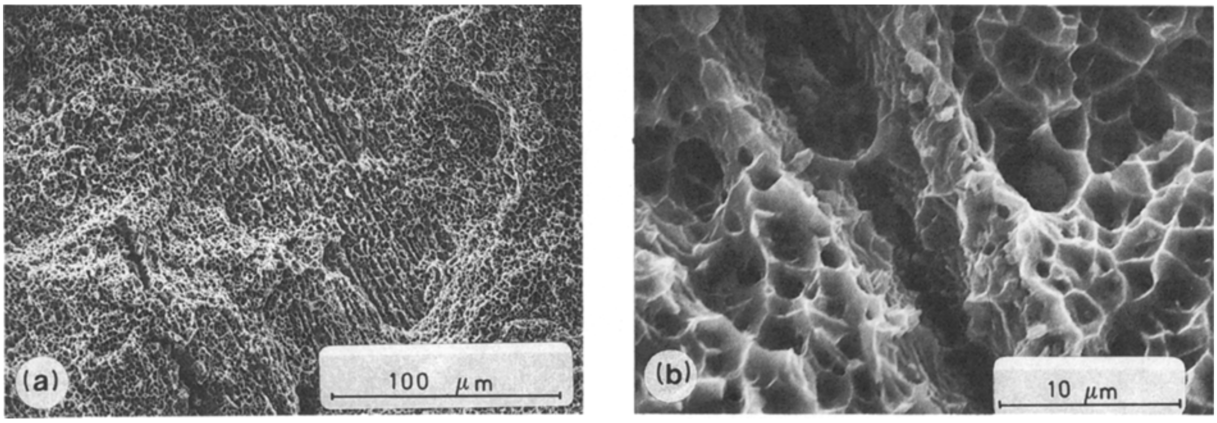

Figure 10 SEM images of fracture surfaces of type 316 stainless steel root-deposit E specimens fractured at room temperature at: (a) low and (b) high magnification.

failure in specimens D and, consequently, to lower total elongation values in specimens E, especially at 400° C.

4.6. Design-oriented data

Although, as is well known [1], the mechanical data from one austenitic weld are not easily applicable to another similar welding, accurate knowledge of such data is useful because it increases the volume of data on austenitic weld deposits which are suitable for statistical analyses for engineering code rules purposes.

In order to obtain design-oriented information on the tensile behaviour of the present weld metal and of the parent metal, the usual engineering properties measured in a tensile test are not sufficient and it is necessary to use analytical expressions which represent all the stress–strain curves (more exactly the true stress–true strain data). We took into consideration the most-used constitutive equations of the plastic flow of the type $\sigma = \sigma(\varepsilon_p)$ where σ is the true stress and ε_p the true plastic strain, supposing that the strain rate and the temperature are fixed (Hollomon [41], Voce [42], Ludwik [43] and Ludwigson [44])

$$\sigma = K_h \varepsilon_p^{n_h} \qquad \text{(Hollomon law)} \quad (1)$$

$$\sigma = B_v \exp(C_v \varepsilon_p) + A_v \qquad \text{(Voce law)} \quad (2)$$

$$\sigma = B_l \varepsilon_p^{n_l} + A_l \qquad \text{(Ludwick law)} \quad (3)$$

$$\sigma = A_{lw} \exp(C_{lw} \varepsilon_p) + K_{lw} \varepsilon_p^{n_{lw}} \qquad \text{(Ludwigson law)} \quad (4)$$

where K_h, A_v, B_v, C_v, A_l, B_l, K_{lw}, A_{lw}, C_{lw} are material constants and n_h, n_l and n_{lw} are strain hardening exponents. The coefficients which appear in these equations were determined by a non-linear statistical analysis based on the least-squares method following the SAS computer system [45]. The results reported in Table IV and also in some plots (Fig. 11) show from a comparison of the standard error of estimate (S.E.) that

(a) the Hollomon law does not give a good description of the plastic flow exhibited by both weld and parent metal. This result confirms the statement that the Hollomon law gives an inadequate representation of the plastic flow of austenitic stainless steels [46–48]. This statement was recently confirmed by a non-linear statistical fit of Equation 1 of experimental data for AISI 316 [14, 15]. Indeed, only at high temperature ($\geqslant 800°$ C) can the Hollomon equation be applied with some accuracy [14, 15];

(b) the Voce law gives the smallest estimate of standard error for the base metal over the plastic range investigated, thus confirming the above-mentioned results [14, 15], even if at very low plastic strain ($\geqslant 0.2$) a slight deviation is shown (see Fig. 11 representing the relative differences between true stress values and work-hardening law fits for tests at room temperature and at $\dot{\varepsilon} = 1 \times 10^{-3}\,\text{sec}^{-1}$);

(c) on the contrary, for the weld metal the best fitting is given by the Ludwick law even if the Voce and Ludwigson laws have a standard error comparable with that of the law mentioned above, but generally higher.

The reason why the fit of the Hollomon Equation 1 is poor with austenitic stainless steels at room and moderate temperature can be found in the presence in the early part of straining of an approximate linear strain-hardening, stage II of the three stages of work-hardening observed in metals (stage I or the easy glide region is observed only in single crystals). This stage is characterized by planar arrays of dislocations while stage III corresponds to a cross-slip cell formation. In lower stacking fault-free energy (SFE) metals and alloys such as stainless steels, dislocations cross-slip with difficulty and the dominant mode observed is stage II. At high temperature the SFE energy increases and stage III (parabolic stage) becomes dominant in turn. Then Equation 1 becomes valid at very high temperatures.

5. Conclusions

A thick section, multipass, submerged-arc weld-deposited metal, type 316 stainless steel, has been investigated by tensile tests at room temperature and at 400° C and by microstructural and compositional analyses of selected fractured all-weld metal specimens. The results indicate the following points.

1. The as-deposited metal has a higher yield strength, a comparable ultimate tensile strength, a lower total elongation than the (as-solution annealed) parent plate. Moreover, the behaviour of the true stress–true strain curves shows a lower strain-hardening capacity in yield-deposited metal as compared to parent metal.

TABLE IV Constants for fitting tensile curves for type 316 stainless steel (base and weld metal) to work-hardening laws

Material	Experimental data		Work hardening law															
	Temp., T (°C)	Strain rate, $\dot{\varepsilon}$ (sec^{-1})	Hollomon			Voce				Ludwik				Ludwigson				
			K_h MPa	n_h	S.E. (MPa)	A_v MPa	B_v MPa	C_v	S.E. (MPa)	A_l MPa	B_l MPa	n_l	S.E. (MPa)	A_{lw} MPa	C_{lw}	K_{lw} MPa	n_{lw}	S.E. (MPa)
Base-metal type 316	20	1×10^{-3}	1251.44	0.37	21.29	1245.90	−949.63	−2.61	1.33	249.60	1263.76	0.67	5.04	245.27	−0.27	1320.11	0.67	5.17
	400	1×10^{-3}	1250.00	0.51	14.04	1189.78	−1029.70	−2.38	2.79	123.55	1339.31	0.72	5.87	149.91	−0.13	1398.99	0.78	7.12
Weld-deposited type 316	20	1×10^{-2}	882.31	0.13	27.77	1092.12	−593.99	−2.61	2.34	488.69	894.71	0.79	2.22	488.74	−0.11	942.74	0.80	2.29
		1×10^{-3}	906.07	0.15	30.69	1217.74	−736.20	−2.02	1.21	472.84	934.89	0.81	1.19	473.09	−0.14	996.55	0.82	5.80
		1×10^{-4}	943.31	0.16	30.15	1233.43	−749.72	−2.03	2.05	472.07	935.30	0.79	1.23	474.48	−0.18	1036.83	0.84	1.46
	400	1×10^{-2}	662.73	0.13	12.98	669.45	−297.97	−4.74	1.39	356.06	586.89	0.66	0.66	357.16	−0.39	701.13	0.70	0.66
		1×10^{-3}	696.38	0.15	12.87	716.15	−354.71	−4.21	1.23	345.81	672.23	0.69	0.89	347.16	−0.37	781.57	0.72	0.91
		1×10^{-4}	765.87	0.17	15.71	849.25	−475.10	−3.21	1.40	362.24	792.16	0.74	0.73	360.12	−0.27	876.65	0.76	0.74

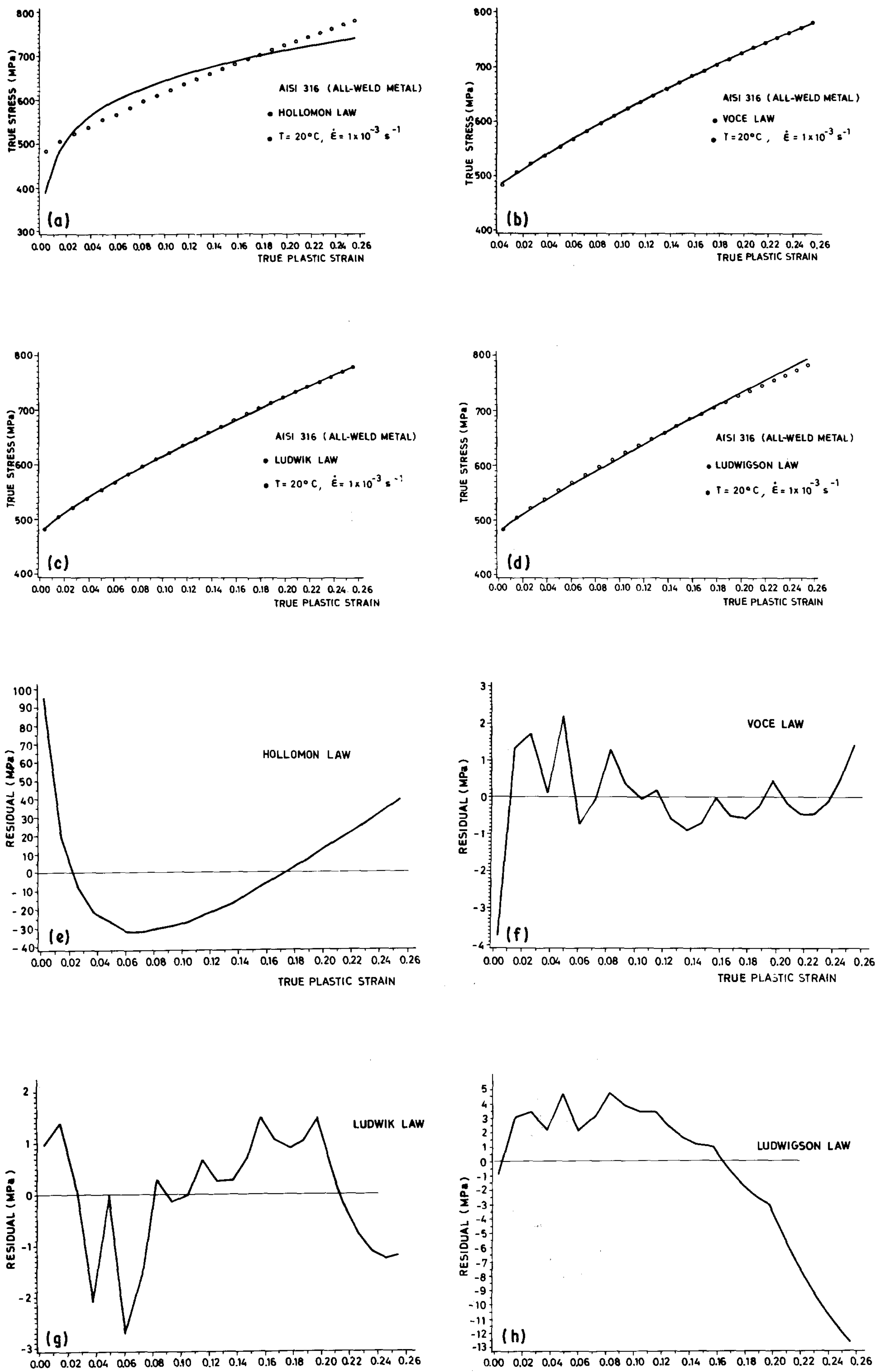

Figure 11 Fitting of the true stress–true strain data from all-weld metal tests to Equations 1 to 4 and relative deviations from the equations: (a, e) Hollomon law; (b, f) Voce law; (c, g) Ludwik law; (d, h) Ludwigson law.

2. Tensile properties vary systematically through the thickness of the weld-deposited metal with the centre of the weld characterized by higher strength and lower ductility than the weld metal near to surfaces.

3. The variations observed are related to an important material variability from the surfaces to the centre of the weld metal characterized mainly by differences in dislocation density caused by local dissimilarities in thermal and mechanical histories during welding and in sub-grain size. Effects due to δ-ferrite (content, distribution and morphology) and chemistry are much less important than to variations in other components such as columnar grain size, sub-grain size.

4. Anisotropy of deformation on the weld metal occurs with a distorsion of the initial circular specimen cross-section into an elliptical one, as a result of preferred orientation developed in the fusion zone during grain growth and enhanced by the occurrence of a "tear-shaped" weld-pool solidification process.

5. The fitting of the true stress–true strain data from tests to several work-hardening laws (Hollomon, Voce, Ludwik and Ludwigson) for design-oriented information purposes shows, from a comparison of the standard error of the estimate, that the Voce and Ludwick equations are the best mathematical descriptions of the data for the parent and the weld metal, respectively.

Acknowledgements

The careful experimental work of M. Airola and H. A. Weir is greatly appreciated. We also thank G. A. Franzetti, G. P. Ossola and Mrs Romor for their contributions. The TEM analysis was performed at the CNR-ITM laboratories (Cinisello Balsamo, Milan, Italy) by F. Gherardi.

References

1. R. T. KING, D. A. CANONICO and C. R. BRINKMAN, *Welding J.* **54** (1975) 265-s.
2. K. H. KLOOS, J. GRANACHER and W. SCHIEBLICH, CEC Report RAP-044D, Commission of the European Communities, Brussels (1983).
3. R. T. KING, J. O. STIEGLER and G. M. GOODWIN, *Welding J.* **53** (1974) 307-s.
4. A. L. WARD, *Nucl. Technol.* **24** (1974) 201-s.
5. J. M. STEICHEN and A. L. WARD, *Welding J.* **54** (1975) 130-s.
6. R. C. BERGREEN *et al.*, *ibid.* **57** (1978) 167-s.
7. C. A. P. HORTON, P. MARSHALL and R. G. THOMAS, in "Proceedings of the International Conference on Mechanical Behaviour and Nuclear Applications of Stainless Steels at Elevated Temperatures", Varese, Italy, 1981 (The Metals Society, London, 1982) Book 280, p. 66.
8. J. R. FOULD and J. MOTEFF, *Welding J.* **61** (1982) 189-s.
9. J. R. FOULD *et al.*, *Metall. Trans.* **14A** (1983) 1357.
10. I. GOWRISANKAR *et al.*, *Welding J.* **66** (1987) 147.
11. W. J. MILLS and L. A. JAMES, *Trans. ASME J. Press. Vessel Technol.* **109** (1987) 336.
12. G. PIATTI and M. VEDANI, *J. Mater. Sci.* **24** (1989) 1429.
13. D. S. WOOD, in "Proceedings of the International Conference on Mechanical Behaviour and Nuclear Applications of Stainless Steels at Elevated Temperatures", Varese, Italy, 1981 (The Metals Society, London, 1982) Book 280, p. 238.
14. S. MATTEAZZI *et al.*, Transactions of the 6th International Conference SMIRT, Vol. L, Paris, 1981 (North-Holland, Amsterdam, 1981) paper 4/7.
15. S. MATTEAZZI, G. PIATTI and D. BOERMAN, in "Proceedings of the International Conference on Mechanical Behaviour and Nuclear Applications of Stainless Steels at Elevated Temperatures", Varese, Italy, 1981 (The Metals Society, London, 1982) Book 280, p. 194.
16. C. ALBERTINI and M. MONTAGNANI, *ibid.*, p. 47.
17. R. A. FARRAR and R. G. THOMAS, *J. Mater. Sci.* **18** (1983) 3461.
18. S. POLGARY, in "Proceedings of the International Conference on Stainless Steels '84", Gothenburg, Sweden, 1984 (The Institute of Metals, London, 1985) Book 320, p. 286.
19. P. MARSHALL, "Austenitic Stainless Steels" (Elsevier Applied Science, New York, 1984) p. 117.
20. K. J. IRVINE, T. GLADMAN and F. B. PICKERING, *J. Iron Steel Inst.* **199** (1961) 153.
21. D. TABOR, *J. Inst. Metals* **79** (1951) 1.
22. I. R. KRAMER, *Trans. AIME* **239** (1967) 1754.
23. J. G. KAUFMAN and R. E. DAVIES, *Mater. Res. Stand.* **10** (1970) 20.
24. G. PIATTI and P. SCHILLER, *J. Nucl. Mater.* **141–143** (1986) 417.
25. W. F. SAVAGE, C. D. LUNDIN and T. F. CHASE, *Welding J.* **47** (1968) 522-s.
26. G. J. DAVIES and J. G. GURLAND, *Int. Metall. Rev.* **20** (1975) 83.
27. S. KOU and Y. LE, *Metall. Trans.* **19A** (1988) 1075.
28. N. SUUTALA, T. TAKALO and T. MOISIO, *ibid.* **10A** (1979) 512.
29. S. A. DAVID, *Welding J.* **60** (1981) 63-s.
30. J. K. LAI *et al.*, in "Conference on Welding and Fabrication in Nuclear Industry" (BNES, London, 1979) Paper 30.
31. F. B. PICKERING, in "Proceedings of the International Conference on Stainless Steels '84", Gotherburg, Sweden, 1984 (The Institute of Metals, London, 1985) Book 320, p. 2.
32. K. J. IRVINE, T. GLADMAN and F. B. PICKERING, *J. Iron Steel Inst.* **207** (1969) 1017.
33. J. A. BROOKS, A. W. THOMPSON and J. C. WILLIAMS, *Welding J.* **63** (1984) 21-s.
34. R. G. THOMAS and S. R. KEOWN, in "Proceedings of the International Conference on Mechanical Behaviour and Nuclear Applications of Stainless Steels at Elevated Temperatures", Varese, Italy, 1981 (The Metals Society, London, 1982) Book 280, p. 30.
35. C. D. BEACHEM and D. A. MEYN, "Electron Fractography", STP 436 (ASTM, Philadelphia, 1979) p. 59.
36. R. H. VAN STONE *et al.*, *Int. Metall. Rev.* **30** (1985) 157.
37. H. G. WILSDORF, *Mater. Sci. Engng* **59** (1983) 1.
38. H. ASTROM *et al.*, *Metal. Sci.* **10** (1976) 225.
39. C. E. LYMAN, *Welding J.* **58** (1979) 189-s.
40. R. A. FARRAR, C. HUELIN and R. G. THOMAS, *J. Mater. Sci.* **20** (1985) 2828.
41. J. HOLLOMON, *Trans. AIME* **162** (1945) 268.
42. E. VOCE, *J. Inst. Metals* **74** (1948) 537.
43. P. LUDWIK, "Elemente der Technologischen Mechanik" (Springer Verlag, Berlin, 1909) p. 32.
44. D. C. LUDWIGSON, *Metall. Trans.* **2** (1971) 2825.
45. SAS Introductory guide (SAS Institute, Cary, North Carolina, 1985).
46. J. R. LOW and F. GAROFALO, *Proc. Soc. Stress Anal.* **4** (1947) 16.
47. W. TRUZKOWSKI, *Mem. Sci. Rev. Mét.* **77** (1980) 193.
48. G. PIATTI, in "Meccanica dei Materiali", edited by L. Lazzarino and E. Manfredi (ETS Editrice, Pisa, 1988) p. 165.

Received 26 April
and accepted 20 October 1989